MAGNETIC RESONANCE IN CHEMISTRY
Magn. Reson. Chem. 2007; **45**: S231–S246
Published online in Wiley InterScience
(www.interscience.wiley.com) DOI: 10.1002/mrc.2159

MRC

Environmentally friendly flame retardants. A detailed solid-state NMR study of melamine orthophosphate

Andreas Brinkmann,[1]* Victor M. Litvinov[2] and Arno P. M. Kentgens[1]

[1] Physical Chemistry/Solid State NMR, Institute for Molecules and Materials, Radboud University Nijmegen, Toernooiveld 1, 6525 ED Nijmegen, The Netherlands
[2] Solid-State NMR, DSM Resolve, 6160 MD Geleen, The Netherlands

Received 16 July 2007; Revised 30 October 2007; Accepted 2 November 2007

We used solid-state NMR spectroscopy to gain detailed information about the proton positions, proximities and the hydrogen-bonding network in the environmentally friendly flame retardant melamine orthophosphate (MP). High-resolution proton one- and two-dimensional solid-state NMR spectra were obtained at high external magnetic field in combination with fast magic angle spinning of the sample. Furthermore, we recorded homo- and heteronuclear correlation spectra of types $^{15}N-^{15}N$, $^{1}H-^{13}C$, $^{1}H-^{15}N$ and $^{1}H-^{31}P$. In addition, we determined the geometry of the NH and NH_2 groups in MP by $^{15}N-^{1}H$ heteronuclear recoupling experiments. We were able to completely assign the different isotropic chemical shifts in MP. Furthermore, we could identify the protonation of the melamine and orthophosphate moieties. The experimental results are discussed in connection with the structural model obtained by powder X-ray diffraction together with a combined molecular modeling-Rietveld refinement approach (De Ridder *et al. Helv. Chim. Acta* 2004; 87: 1894). We show that the geometry of the NH_2 groups can only be successfully estimated by solid-state NMR. Copyright © 2007 John Wiley & Sons, Ltd.

KEYWORDS: solid-state NMR; ^{1}H; ^{13}C; ^{15}N; ^{31}P; environmentally friendly flame retardants; melamine phosphates; heteronuclear correlation spectroscopy; homonuclear double-quantum spectroscopy; distance measurements

INTRODUCTION

Materials based on natural and synthetic polymers are used in a wide range of areas. The fire hazards associated with these materials require the use of flame retardants for many applications, in order to reduce the combustibility of the polymers. Flame retardants interfere at a particular stage with the combustion process and may be classified according to whether they act physically or chemically, in the gas or condensed phase.[1,2]

Halogen-containing flame retardants act in the gas phase by chemically interfering with the radical chain mechanism during combustion. Although halogenated compounds are widely used, they suffer from clear disadvantages: The hydrogen halides, like HCl and HBr, formed during combustion are highly toxic and corrosive. In addition, brominated flame retardants and their combustion products have been identified to contaminate the environment on a wide scale and to be harmful to humans by accumulating through food chains.[2,3]

Therefore, the development of nonhalogenated flame retardants has received increasing attention in the last years.[1,2] These compounds generally act in the condensed phase by promoting the formation of a char layer on the polymer surface, which acts as an insulating barrier to shield the polymer surface against heat and air. Furthermore, the diffusion of gaseous products to the flame is inhibited. A condensed phase flame retardant is in addition called *intumescent*, if the polymer material swells when exposed to fire or heat to form a porous foamed char layer, which acts as the barrier.[1] Intumescence can be achieved by using nitrogen and nitrogen–phosphorus-based compounds as flame retardants, which in addition are considered to be environmental friendly.[4] One compound of this type is ammonium polyphosphate. Other important examples are melamine orthophosphates (MPs), melamine pyrophosphates (MPys) and melamine polyphosphates (MPolys), which are already commercially available, but more applications and a detailed understanding of their flame-retarding mechanism is needed. In order to improve flame retardants based on melamine phosphates, it is essential to relate their chemical composition and structure to their functional mechanism.

Although melamine has a low solubility in water,[5] it forms crystals of sufficient size from water so that its crystal structure could be determined by X-ray[6] and neutron diffraction.[7] A large number of melamine salts formed with inorganic and organic acids have been described in the literature.[5,8] Since many of these salts crystallize well, their crystal structures could be determined straightforwardly (for an overview see for example Ref. 8). One interesting feature of these structures is the dense hydrogen bond

*Correspondence to: Andreas Brinkmann, Physical Chemistry/Solid State NMR, Institute for Molecules and Materials, Radboud University Nijmegen, Toernooiveld 1, 6525 ED Nijmegen, The Netherlands. E-mail: A.Brinkmann@science.ru.nl

system, which comprises strong and weak hydrogen bonds of the types N–H···N, N–H···O and O–H···O following the classification of hydrogen bond strength according to Ref. 9. These types of hydrogen bonds are a determining factor for the molecular self-organizing processes in these materials.[8]

Melamine phosphates are the salts formed by melamine with phosphoric acid, shown in Fig. 1(a) and (b). MP can be obtained by using orthophosphoric acid. The condensed phosphates may in general be obtained by two different approaches: Firstly, heating MP leads to its gradual condensation into MPy and MPoly, under which water is expelled. Secondly, pyro- and polyphosphoric acid may be used to obtain MPy and MPoly directly.[10]

Recently, the structures of a four melamine phosphates have been solved.[11–14] Whilst $M_6P_5(H_2O)_4$ crystallizes well and allows single-crystal X-ray diffraction,[12] MP,[11] MPy[13] and MPoly[14] just form micro crystals so that a combined approach of high-resolution synchrotron powder diffraction, solid-state nuclear magnetic resonance (NMR) spectroscopy and molecular modeling is required. In this contribution, we present the solid-state NMR results obtained on MP and pinpoint key structural features that allowed us to come to the structural model of MP presented in Ref. 11.

Solid-State NMR, especially when combined with isotopic labeling, is capable of extracting molecular structural information in systems that do not possess long-range order (crystallinity). Since the anisotropic spin interactions lead to NMR spectra of low sensitivity and resolution for static disordered samples, these applications require magic angle spinning (MAS), where the sample is rapidly rotated about an axis at the magic angle (≈54.74°) with respect to the static magnetic field. Solid-state NMR methods have been developed that allow determining not only molecular structural parameters such as internuclear distances, bond angles and torsional angles but also characterizing hydrogen bonding.[15–19] ^{1}H solid-state NMR is ideal to characterize hydrogen bonding, since it allows direct detection of the nuclei forming hydrogen bonds. The proton chemical shift is very sensitive to the strength of the hydrogen bond. In addition, solid-state NMR allows to directly determine ^{13}C–^{1}H, ^{15}N–^{1}H and ^{17}O–^{1}H distances[18,20–26] via the heteronuclear dipolar couplings, either quantitatively or more qualitatively via two-dimensional (2D) through-space heteronuclear correlation (HETCOR) spectroscopy.[27] The latter correlates the chemical shift of nuclei that are in close spatial proximity.

High-resolution ^{1}H NMR in solids is not an easy task, since the strong network of homonuclear ^{1}H dipolar couplings leads to broad, spectral lines without any detailed structure. MAS at low and intermediate spinning frequencies fails to average these homonuclear dipolar couplings completely and does not achieve well-resolved spectra. Combining MAS with applying sequences of radiofrequency pulses to the ^{1}H spins leads to enhanced averaging of the ^{1}H homonuclear dipolar couplings (*homonuclear decoupling*) and hence to improved resolution and sensitivity in the resulting ^{1}H spectra.[28] Furthermore, in recent years NMR probes have been developed that allow sample spinning up to 70 kHz, which is sufficient to considerably improve the proton spectral resolution.[29] In addition, high external

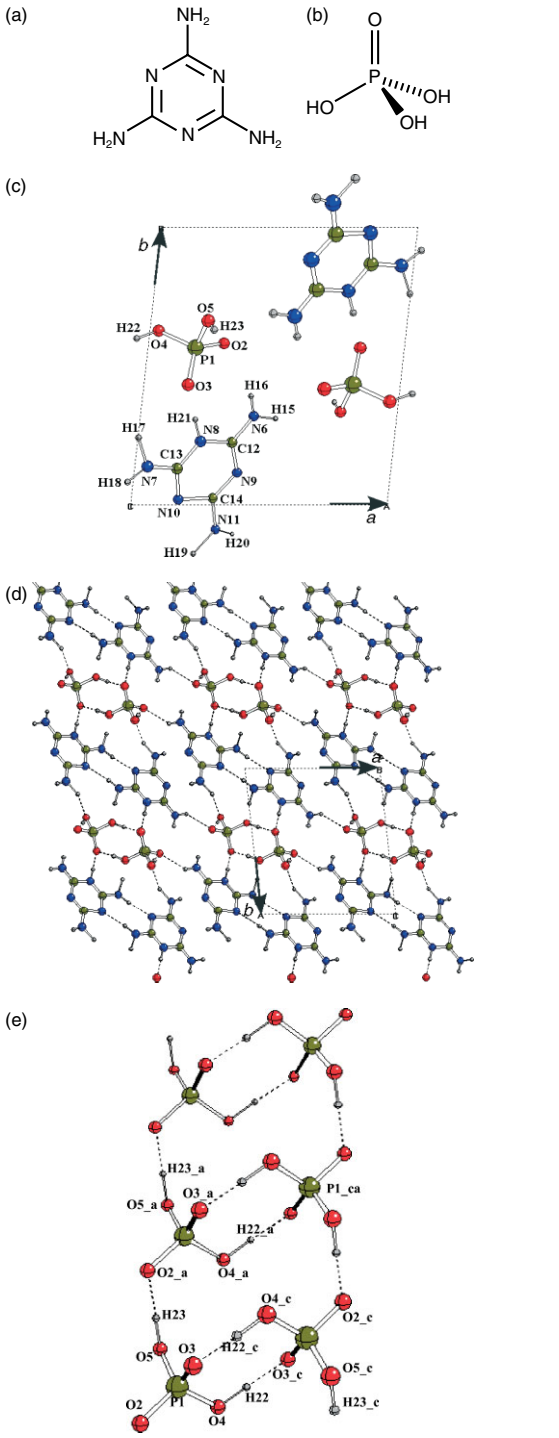

Figure 1. Chemical structures of (a) melamine and (b) phosphoric acid. (c) X-ray structure of MP obtained by synchrotron powder diffraction together with a combined molecular modeling-Rietveld refinement approach.[11] The atomic numbering scheme of MP in the asymmetric part of the unit cell viewed along the $-c$ crystallographic direction is shown. (d) Crystal packing of MP viewed along the $+c$ direction showing the hydrogen bonding in the melamine ribbons and the pairs of $H_2PO_4^-$ groups. (e) Pairs of phosphate chains (in vertical direction) in MP. Subscripts a, c and ca correspond to symmetry operations (x, y, $1-z$), ($-x$, $1-y$, $1-z$), and ($-x$, $1-y$, $2-z$) respectively. (c)–(e) are reprinted with permission from Ref. 11. Copyright 2004, Schweizerische Chemische Gesellschaft.

DOI: 10.1002/mrc

magnetic fields (up to 21 T) allow to pull apart overlapping proton resonances. Hence, the combination of high external fields together with fast MAS leads to well-resolved proton spectra with a high sensitivity, which allow the assignment of proton resonances and identify participants in hydrogen bonding. For example, ^{1}H solid-state NMR and ^{15}N–^{1}H distance measurements have been successfully used to study hydrogen bonding in self assembling materials such as benzoxazine oligomers[30] and multiple hydrogen-bonded dimers taking the form of pyrimidinone or pyrimidinol.[23,31]

Solid-state NMR has been used before to study materials based on melamine. Damodaran *et al*. investigated melamine and cyanuric acid-melamine systems by one-dimensional ^{13}C, ^{15}N and ^{2}H spectroscopy.[32] Schnick and coworkers performed ^{13}C and ^{15}N experiments on melamine, melam, melem and melon, where the latter three are examples of condensated melamine, representing graphitic forms of carbon nitrides.[33–35] In addition, they determined the structure of the melem adduct with orthophosphoric acid, in which no phosphate salt is formed, i.e. no transfer of protons from the orthophosphoric acid to the melem molecule takes place.[36] Jahromi *et al*. performed simple one-dimensional ^{13}C and ^{31}P spectroscopy on MP, MPy, MPoly and mixtures of MPoly with polyamides[37] Our recent studies of the structure of MPy and MPoly included high-resolution ^{1}H spectroscopy, ^{31}P spectroscopy and ^{31}P–^{1}H HETCOR spectroscopy.[13,14]

In view of possible mechanistic studies of the process underlying the flame-retardant capabilities of melamine phosphates, an in-depth characterization of the base material is essential. In this contribution, we apply a host of solid-state NMR techniques to gain detailed information about the proton positions, proximities and the hydrogen-bonding network in MP. We present and discuss high-resolution ^{1}H single- and ^{1}H–^{1}H double-quantum spectra, heteronuclear and homonuclear correlation spectra of types ^{1}H–^{13}C, ^{1}H–^{15}N, ^{1}H–^{31}P, and ^{15}N–^{15}N. Furthermore, we determine ^{15}N–^{1}H distances.

RESULTS

One-dimensional spectra

Figure 2(a) shows the one-dimensional (1D) single-scan ^{1}H spectrum of MP obtained at an external field of 18.8 T and fast magic angle sample spinning with a frequency of 49.1 kHz. The spectrum contains two broad lines in the chemical shift range 4–10 ppm. Three resonances appear in the chemical shift range 10–16 ppm assigned to protons involved in O–H···O or N–H···O type of hydrogen bonding: A well-separated resonance at 11.1 ppm and two overlapping resonances at 13.2 and 13.7 ppm.

Both Jürgens *et al*. and Damodaran *et al*. have measured ^{13}C and ^{15}N cross-polarization magic angle spinning (CP-MAS) spectra of melamine.[32,33] The chemical structure of melamine is shown in Fig. 1(a). The ^{13}C CP-MAS spectrum of melamine contains two resonances at 167.5 and 169.2 ppm with an intensity ratio of about 2 : 1 (spectrum not shown here).[33] Owing to the varying cross-polarization (CP) efficiency for different chemical sites, CP experiments may not in general be interpreted quantitatively. However, since all three ^{13}C sites in the melamine molecule are of the same type, the CP experiment can give a rough estimate about the multiplicity of the chemical sites contributing to different resonance lines. This shows that in solid melamine the three carbon sites are not magnetically equivalent as they are in melamine dissolved in DMSO.[33] This inequivalence in solid melamine results from ring current shifts by the packing of the melamine rings.

In MP, this inequivalence becomes significantly stronger as is evidenced by the ^{13}C CP-MAS spectrum of [U-^{13}C]-MP shown in Fig. 2(b). It shows two ^{13}C resonances at 156 and 164 ppm again with an intensity ratio of about 2 : 1. The strong

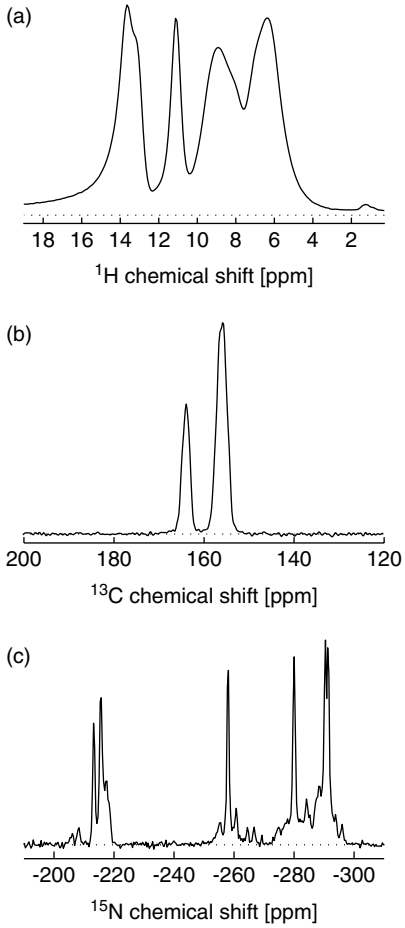

Figure 2. (a) The experimental single-pulse ^{1}H magic angle spinning solid-state NMR spectrum of MP shows five main resonances. The two broad lines in the chemical shift range 4–10 ppm stem from the NH_2 groups. Three resonances appear in the chemical shift range (10–16 ppm) of protons involved in hydrogen bonding. They stem from H atoms bonded to the phosphate oxygen atoms (11.1 and 13.2 ppm) and from one H atom bonded to an endocyclic ring N-atom (13.7 ppm). The spectrum was obtained at a static field of 18.8 T and a sample spinning frequency of 49.1 kHz. (b) Experimental ^{13}C CP-MAS spectrum of [U-^{13}C]-MP recorded at an external field of 7.05 T and a sample spinning frequency of 12 kHz. (c) Experimental ^{15}N CP-MAS spectrum of [U-^{15}N]-MP obtained at an external field of 7.05 T and a sample spinning frequency of 12 kHz.

DOI: 10.1002/mrc

inequivalence indicates that in MP the chemical surrounding of one carbon site is significantly different from that of the two other carbon sites, which can no longer be attributed to ring current shifts induced by neighboring melamine rings. The relatively large linewidth of about 160 and 210 Hz of the two resonances at 164 and 156 ppm respectively are most likely caused by the residual dipolar couplings of the ^{13}C nuclei to the surrounding ^{14}N nuclei. It has been shown by Orr and Duer that pulsed ^{14}N decoupling can give enhanced ^{13}C sensitivity and reduced ^{13}C line widths.[38]

The ^{15}N CP-MAS spectrum of [U-^{15}N]-melamine (results not shown) contains three resonance lines at −205.7, −207.8 and −209.7 ppm (indirectly referenced to nitromethane) assigned to the three nonprotonated endocyclic nitrogens and three resonance lines at −289.0, −292.6 and −296.3 ppm assigned to the three exocyclic NH_2 groups. Our results are in agreement with those obtained by Damodaran *et al*.[32] but differ slightly from the ones obtained by Jürgens *et al*.[33]

The ^{15}N CP-MAS spectrum of [U-^{15}N]-MP is shown in Fig. 2(c) changes significantly when compared to the one of melamine. Two resonances remain in the spectral region of the nonprotonated endocyclic nitrogens but are shifted to −213.3 and −215.6 ppm. One resonance line is shifted significantly to −258.0 ppm indicating a protonated endocyclic nitrogen. Three resonances remain in the spectral region of the NH_2 groups where two are lying quite close together with chemical shifts of −290.5 and −291.3 ppm, indicating two NH_2 groups with a similar chemical surrounding, whereas one resonance is shifted further away to −280.0 ppm, indicating a clear difference in chemical surrounding of this NH_2 group compared to the other two NH_2 groups. We attribute the additional smaller lines and broad feet in the ^{15}N spectrum to possible impurities resulting from the synthesis of [U-^{15}N]-melamine and [U-^{15}N]-MP, and disorder in the MP sample. Condensation products of melamine such as melam, melem and melon are known to occur as a result of the heat treatment during synthesis.[34] The chemical shifts observed neither directly correspond to those of pure melam,[34] melem[33] and melon[35] nor those of the adduct of melem with orthophosphoric acid.[36] However, it is unclear whether the impurities are other types of carbon nitrides or their phosphate salts.

Two-dimensional heteronuclear correlation spectroscopy

To gain further insight into the spatial proximities of the nuclei connected to the various observed resonances and thus get a more detailed structural picture, a series of two-dimensional HETCOR experiments were conducted.

Figure 3(b) shows an experimental 2D ^{1}H–^{13}C HETCOR spectrum obtained on [U-^{13}C]-MP at a static field of 7.05 T and a spinning frequency of 12 kHz using the radio frequency (rf) pulse sequence shown in Fig. 11(a) that is discussed in detail in the section materials and methods. The high-resolution ^{1}H dimension is obtained by frequency-switched Lee–Goldburg (FSLG) homonuclear decoupling in the indirect time dimension t_1. After the proton magnetization is transferred to ^{13}C by Lee–Goldburg cross-polarization (LG-CP), the signal ^{13}C signal is detected in the direct time dimension t_2. Cross peaks in the resulting 2D spectra indicate through-space ^{1}H–^{13}C magnetization transfer between the corresponding spins via the heteronuclear dipolar couplings, hence cross peaks indicate ^{13}C–^{1}H close through-space contacts.

The spectrum in Fig. 3(b) shows crosspeaks between both ^{13}C lines (at 164 and 156 ppm) and the broad multiple signal component of the ^{1}H spectrum. But only the ^{13}C line at 156 ppm shows a crosspeak to a ^{1}H line at about 13.2 ppm. However, since the crosspeak in the ^{1}H dimension is relatively broad, it is difficult to assign this peak to either the ^{1}H resonance at 13.2 or 13.7 ppm in the 1D ^{1}H spectrum obtained at 18.8 T external field and 49.1 kHz MAS frequency shown for comparison in 3(a). There is clearly no cross peak between either ^{13}C resonances and the ^{1}H resonance at 11.1 ppm. Hence, the ^{13}C sites contributing to the 164 ppm ^{13}C line are far in space from the ^{1}H sites that contribute to the ^{1}H resonances at 11.1, 13.2, and 13.7 ppm. There is no close through-space contact between *any* ^{13}C site and the ^{1}H site contributing to the 11.1 ppm resonance line. This indicates that these protons are not in proximity to the melamine molecule.

Figures 4(b) and (c) show experimental 2D ^{1}H–^{31}P HETCOR spectra obtained on [U-^{13}C]-MP at a static field of 7.05 T and a spinning frequency of 12 kHz using the rf pulse

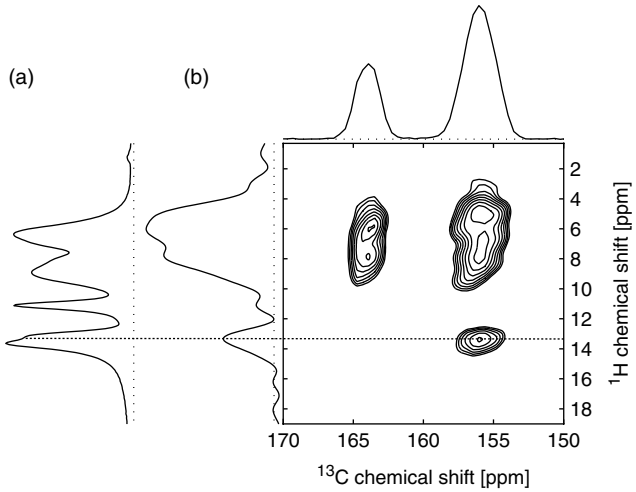

Figure 3. (a) Single-pulse ^{1}H spectrum of MP obtained at 18.8 T and 49.1 kHz MAS frequency. (b) Experimental 2D ^{1}H–^{13}C correlation spectrum of [U-^{13}C]-MP obtained at 7.05 T and 12 kHz MAS frequency, where FSLG homonuclear decoupling was applied in the indirect ^{1}H dimension. The ^{1}H magnetization was transferred to the ^{13}C spins by LG-CP. The FSLG decoupling used a ^{1}H nutation requency of 100 kHz and frequency jumps of ±70.711 kHz with an overall offset of −1.5 kHz. The frequency jumps were performed with a simultaneous 180° phase shift every 8.16 μs. During LG-CP, the ^{1}H nutation frequency was 100 kHz and the rf frequency offset was 70.711 kHz. The nutation frequency of the ^{13}C rf field was optimized to the −1 CP sideband condition. The cross-polarization interval was 0.75 ms. TPPM decoupling with a ^{1}H nutation frequency of 100 kHz, pulse duration of 5.4 μs and rf phases of ±20° was applied during signal detection. The delay between experiments was 6 s.

DOI: 10.1002/mrc

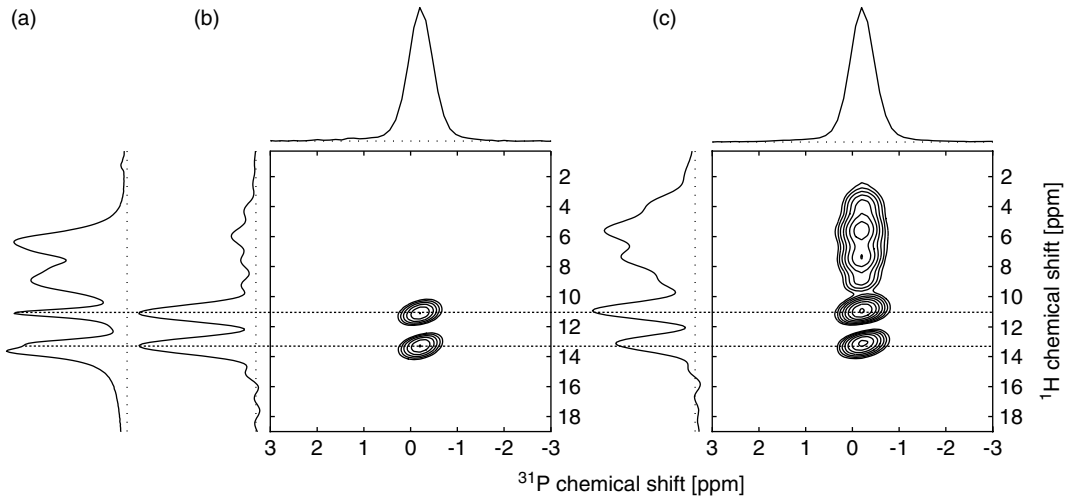

Figure 4. (a) Single-pulse ^{1}H spectrum of MP obtained at 18.8 T and 49.1 kHz MAS frequency. (b) and (c) Experimental 2D ^{1}H–^{31}P correlation spectra of [U-^{13}C]-MP obtained at 7.05 T and 12 kHz MAS frequency, where FSLG homonuclear decoupling was applied in the indirect ^{1}H dimension. The ^{1}H magnetization was transferred to the ^{31}P spins by LG-CP. The same parameters for FSLG and LG-CP were used as given in the caption of Fig. 3. TPPM decoupling with a ^{1}H nutation frequency of 100 kHz, pulse duration of 5.4 μs and rf phases of ±15° was applied during signal detection. The delay between experiments was 6 s. The cross-polarization intervals were (b) 0.1 ms and (c) 2.5 ms.

sequence shown in Fig. 11(a). The fast dynamics of magnetization transfer between the ^{1}H and ^{31}P sites are evident. Two cross peaks are already visible at a cross-polarization time of 0.1 ms : One to ^{1}H resonance at 11.1 ppm and one to a ^{1}H resonance at about 13.5 ppm. Because of the linewidth, it is again difficult to assign this peak nonambiguously to one of the ^{1}H resonances at 13.2 or 13.7 ppm in the high-resolution 1D ^{1}H spectrum shown for comparison in Fig. 4(a). The magnetization transfer to the ^{1}H resonance lines in the range 4–10 ppm is much slower, supporting that the ^{1}H sites with 11.1 and either 13.2 or 13.7 ppm are located close to the ^{31}P spins, indicating attachment to the PO_4 groups.

Figures 5(b) and (c) show experimental 2D heteronuclear ^{1}H–^{15}N spectra obtained on [U-^{15}N]-MP a static field of 7.05 T and a spinning frequency of 12 kHz using the rf pulse sequence shown in Fig. 11(a). Figures 6(c)–(f) show sections through the 2D spectrum shown in 5(b) parallel to the axis of the ^{1}H chemical shift at the position of different ^{15}N resonances. None of the ^{15}N resonances has a cross peak with the ^{1}H resonance at 11.1 ppm, supporting again the conclusion that these protons are likely to be connected to the PO_4 units. Considering the much smaller ^{15}N–^{1}H dipolar couplings in comparison with the ^{31}P–^{1}H dipolar couplings, these cross peaks are only expected to appear at much longer cross-polarization intervals. Only the ^{15}N resonance at −258 ppm has a cross peak with the ^{1}H resonance at 13.2 or 13.7 ppm. This suggests that ^{1}H sites giving rise to the resonance line at about 13.5 ppm are part of an endocyclic NH group in the melamine molecules. Since two proton resonances are visible in the high-resolution spectrum at 13.2 and 13.7 ppm, this suggests that one of the resonances stems from an endocyclic NH proton in the melamine molecule, whereas the other one stems from a proton site attached to the PO_4 groups. The question which of the two ^{1}H resonances at 13.2 and 13.7 ppm originates from the NH group was answered by taking 2D ^{15}N–^{1}H HETCOR spectra at an external field of 18.8 T and a sample spinning frequency of 50 kHz (results not shown). This shows that the ^{15}N resonance at −258 ppm has a cross peak with the ^{1}H resonance at 13.7 ppm but not with the resonance at 13.2 ppm. Hence, the ^{1}H resonance at 13.7 ppm stems from the endocyclic NH group, whereas the ^{1}H resonances at 13.2 and 11.1 ppm stem from the H_2PO_4 proton sites. Furthermore, the ^{15}N resonance at −258 ppm stems from an endocyclic NH site in the melamine moiety. It is clear that the ^{15}N spins, which give rise to the resonance lines at −213.3 and −215.6 ppm, are not in close contact to any ^{1}H spins. This suggests that the corresponding nitrogen sites in the melamine are completely deprotonated, hence they stem from two endocyclic unprotonated nitrogens. The ^{15}N resonances at −280.0, −290.5 and −291.3 ppm are assigned to NH_2 groups in the melamine molecule, which are not hydrogen bonded or in close contact with the PO_4 groups. The sections through the 2D ^{1}H–^{15}N HETCOR spectrum allow a further assignment of ^{1}H chemical shifts. Figure 6(c) shows a correlation of the ^{15}N resonance at −291.3 ppm with two ^{1}H resonances at 8.0 and 6.2 ppm. Figure 6(d) shows a correlation of the ^{15}N resonance at −290.5 ppm with two ^{1}H resonances at 9.1 and 5.6 ppm. Figure 6(e) shows a correlation of the ^{15}N resonance at −280.0 ppm with two ^{1}H resonances at 8.7 and 6.8 ppm.

Two-dimensional homonuclear correlation spectroscopy

Besides establishing heteronuclear correlations, it can be very useful to determine contacts between nuclei of the same atomic species. Especially spectra correlating double-quantum coherences to single-quantum coherences are very useful in identifying spin pairs close in space and give an overview of the connectivities between all nuclei of the same species in a material.

Figure 7 shows an experimental 2D homonuclear double-quantum ^{1}H experiment of MP obtained at an external field

DOI: 10.1002/mrc

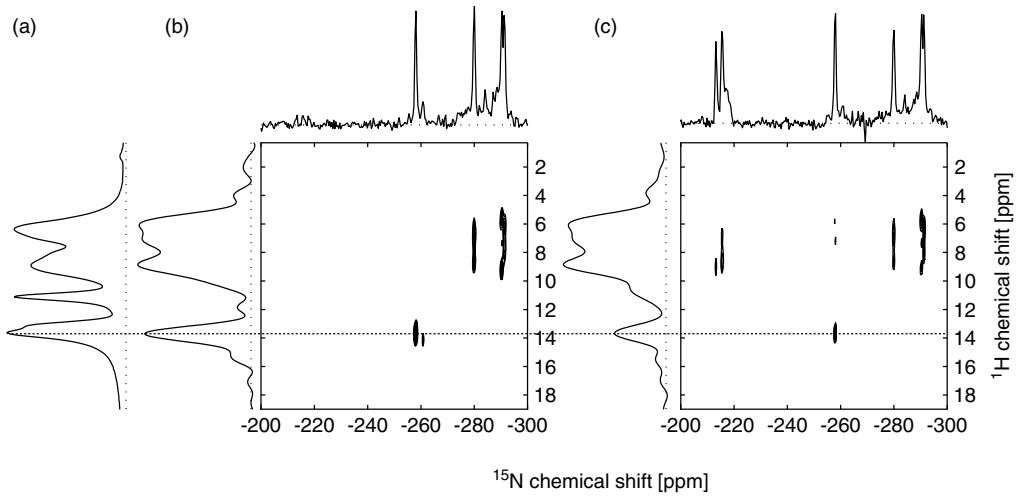

Figure 5. (a) Single-pulse ^{1}H spectrum of MP obtained at 18.8 T and 49.1 kHz MAS frequency. (b) and (c) Experimental 2D ^{1}H–^{15}N correlation spectra of [U-^{15}N]-MP obtained at 7.05 T and 12 kHz MAS frequency, where FSLG homonuclear decoupling was applied in the indirect ^{1}H dimension. The ^{1}H magnetization was transferred to the ^{15}N spins by LG-CP. The same parameters for FSLG and LG-CP were used as given in the caption of Fig. 3. TPPM decoupling with a ^{1}H nutation frequency of 100 kHz, pulse duration of 5.4 μs and rf phases of $\pm 15^{\circ}$ was applied during signal detection. The delay between experiments was 6 s. The cross-polarization intervals were (b) 0.2 ms and (c) 5 ms.

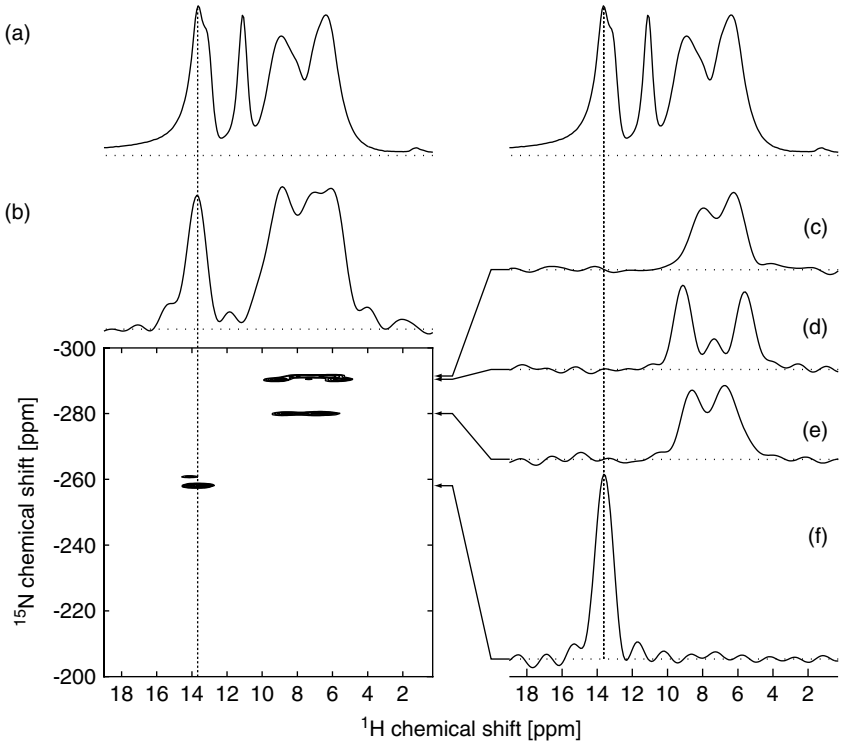

Figure 6. (a) Single-pulse ^{1}H spectra of MP obtained at 18.8 T and 49.1 kHz MAS frequency. (b) Detailed view of the experimental 2D ^{1}H–^{15}N spectrum shown in Fig. 5. Sections through the 2D spectrum parallel to the ^{1}H chemical shift axis at the different ^{15}N resonances are shown on the right.

of 18.8 T and a spinning frequency of 50 kHz using the pulse sequence shown in Fig. 11(b). The ^{1}H double-quantum coherences are excited and reconverted using the C7 sequence[39] employing the basic element from the back-to-back (BABA) sequence.[40,41] The ω_1 dimension of the 2D spectrum corresponds to the ^{1}H double-quantum dimension, whilst the ω_2 dimension corresponds to the ^{1}H single-quantum dimension. Double-quantum peaks in the 2D spectrum indicate a close through-space contact between the the two ^{1}H sites contributing to the double-quantum peak. The solid lines in Fig. 7 represent clear through-space contacts. Double-quantum coherences between identical spin sites appear on the diagonal of the 2D spectrum. This is the case for the ^{1}H resonance at 11.1 ppm. In addition, this resonance shows strong double-quantum peaks with the resonance at 13.7 ppm and a resonance at 6.2 ppm. The resonance at 13.2 ppm shows a double-quantum peak with the resonance at 6.8 ppm. In addition, the ^{1}H resonance at 13.7 ppm shows

DOI: 10.1002/mrc

a double-quantum peak with a resonance at about 8.3 ppm. The broad double-quantum peak between resonances at 9.0 and 6.8 ppm results from the overlap of the double-quantum peaks of all three NH_2 groups.

Finally, to unequivocally assign all the resonances in the various spectra, a 2D homonuclear double-quantum ^{15}N spectrum of [U-^{15}N]-MP was performed as shown in Fig. 8. The spectrum was obtained at an external field of 7.05 T and a sample spinning frequency of 6.056 kHz. We employed the POST-C7 sequence[42] to excite and reconvert ^{15}N double-quantum coherences as shown in Fig. 11(c). The ω_1 dimension of the 2D spectrum corresponds to the ^{15}N double-quantum dimension, whilst the ω_2 dimension corresponds to the ^{15}N single-quantum dimension. Double-quantum peaks in the 2D spectrum indicate a close through-space contact between the the two ^{15}N sites contributing to the double-quantum peak. The solid lines in Fig. 8 represent clear through-space contacts. The ^{15}N resonances at −213 and −215.6 ppm show a double-quantum peak with each other and with the ^{15}N resonances at −258 and −280 ppm. The resonance at −213 ppm shows a double-quantum peak with the resonance at −290.5 ppm, whereas the resonance at −215.6 ppm shows a double-quantum peak with the resonance at −291.3 ppm. In addition, both ^{15}N resonances at −290.5 and −291.3 ppm show a double-quantum peak with the resonance at −258 ppm.

In Fig. 9(a), the results from the homonuclear correlation and HETCOR experiments are summarized in the form of a contact diagram. The chemical shifts of the different ^1H, ^{15}N, ^{13}C and ^{31}P resonances are presented as boxes and connecting solid lines represent close through-space contacts between the corresponding chemical sites. From this diagram, it is clear that during the formation of MP the melamine ring becomes protonated at one of the endocyclic nitrogen

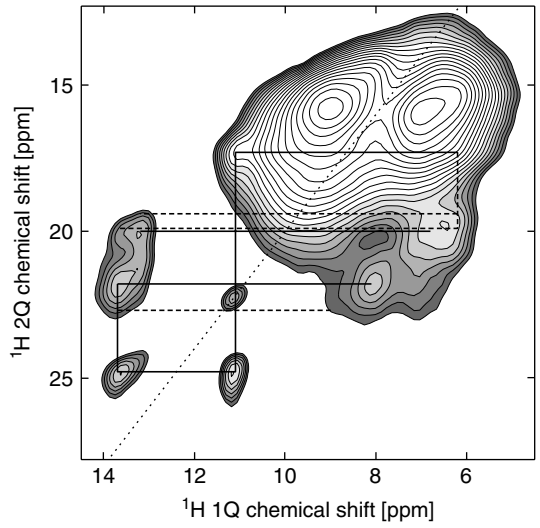

Figure 7. Experimental 2D homonuclear double-quantum ^1H spectrum of MP obtained at an external field of 18.8 T and 50 kHz MAS frequency using the C7 sequence[39] employing a BABA[40,41] basic element (C7-BABA). The strong contacts leading to our suggested assignment of the ^1H resonances are indicated by solid lines. Dashed lines indicate contacts that are in agreement with our assignment.

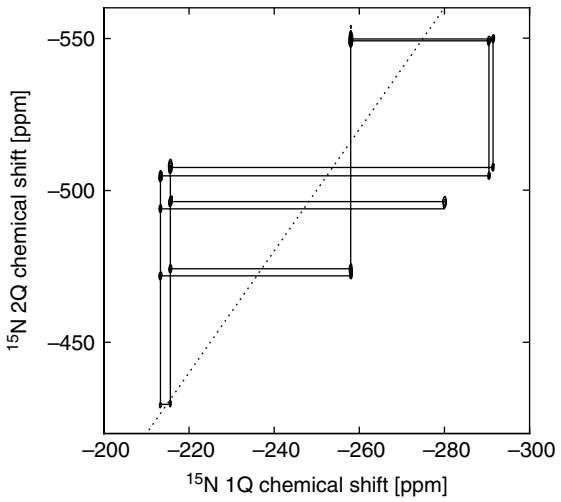

Figure 8. Experimental 2D homonuclear double-quantum ^{15}N spectrum of [U-^{15}N]-MP obtained at an external field of 7.1 T and 6.056 kHz MAS frequency using the POST-C7 sequence.[42] The suggested contacts of the ^{15}N single- and double-quantum coherences are indicated in the spectrum.

positions, whereas the remaining two protons originating from the phosphoric acid are engaged in hydrogen bonds between neighboring phosphate groups. This information was used to calculate a structural model based on the powder X-ray data presented in a previous publication.[11]

$^{15}N-^1H$ distance measurements

Considering the various hydrogen bonds that have been established during the formation of MP and their role in the formation of the molecular arrangement leading to the MP structure, we tried to establish the strength of the various bonds by measuring $^{15}N-^1H$ bond lengths by a 2D separate local field (SLF) experiment.

Figure 10 show experimental result of $^{15}N-^1H$ distance measurements obtained in [U-^{15}N]-MP at an external field of 7.05 T and a sample spinning frequency of 20.578 kHz using the pulse sequence shown in Fig. 11(d). The $R18_2^5$ sequence has been employed to recouple the heteronuclear $^{15}N-^1H$ dipolar couplings while decoupling the homonuclear proton dipolar interactions.[21,22] The experimental 2D spectrum shown in Fig. 10(a) correlates the isotropic ^{15}N chemical shift and the recoupled $^{15}N-^1H$ heteronuclear dipolar coupling. The solid black lines in Fig. 10(b)–(e) correspond to sections through the experimental 2D spectrum parallel to the ω_1 axis (recoupled dipolar coupling dimension) at the spectral positions of the different NH_2 and NH resonances in the ^{15}N chemical shift dimension of the 2D spectrum. The dashed lines are the best-fit results of average Liouville calculations. The details of these calculations and the fitting procedure are described in the section materials and methods. In the case of the NH_2 groups, Fig. 10(b)–(d), a three-spin system consisting of a single ^{15}N and two ^1H sites was assumed. The fitting parameters included the two $^{15}N-^1H$ heteronuclear dipolar couplings and the H–N–H bond angle. In the case of the NH group, Fig. 10(e), a two-spin system consisting of a single ^{15}N and a single ^1H site was assumed, and one of the fitting parameters was the $^{15}N-^1H$ heteronuclear dipolar

DOI: 10.1002/mrc

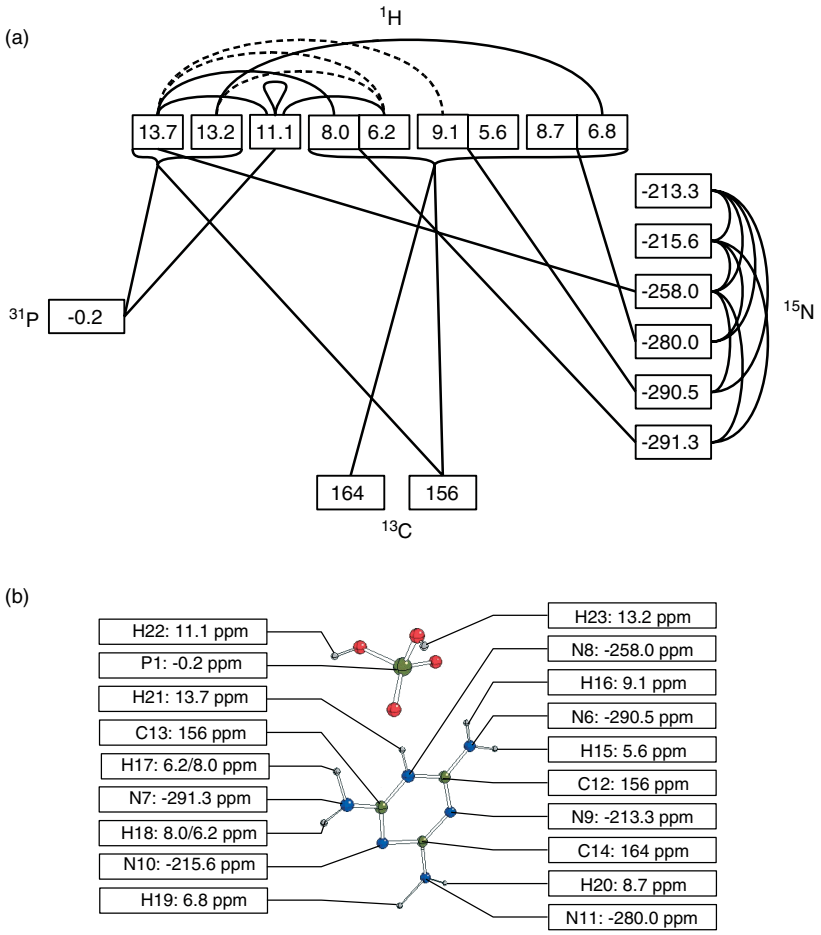

Figure 9. (a) Experimentally determined chemical shifts in ppm of the ^{1}H (top row), ^{15}N (right column), ^{13}C (bottom row) and ^{31}P (left column) resonances of MP. Close through-space contacts determined from the different homonuclear and heteronuclear 2D correlation spectra are indicated by solid lines. The ^{31}P–^{1}H contacts were determined from the 2D HETCOR spectrum shown in Fig. 4, the ^{13}C–^{1}H contacts were derived from the 2D HETCOR spectrum shown in Fig. 3, the ^{15}N–^{1}H contacts were established with the help of the 2D HETCOR spectra shown in Figs 5 and 6, the ^{15}N–^{15}N contacts were ascertained from the 2D homonuclear double-quantum ^{15}N spectrum shown in Fig. 8, and the ^{1}H–^{1}H contacts were determined from the 2D homonuclear double-quantum ^{1}H spectrum shown in Fig. 7. In the latter case, the dashed lines indicate additional contacts that are in agreement with our assignment. (b) Molecular Structure of MP together with the suggested chemical shift assignment.

coupling. The complete set of fitting parameters is given in the section materials and methods.

The results of the geometry determination for the different NH and NH_2 groups in MP are summarized in Table 2. The experimental and simulated dipolar lineshapes for the NH group with a ^{15}N chemical shift of −258.0 ppm are shown in Fig. 10(e). We obtained a heteronuclear dipolar ^{15}N–^{1}H coupling constant of $b_{12}/2\pi = 11\,200$ (−85, +27) Hz, corresponding to an internuclear N–H distance of $r_{12} = 102.8$ (+0.3, −0.1) pm.

The dipolar lineshape results for the NH_2 group at an ^{15}N chemical shift of −291.3 ppm are shown in Fig. 10(b). As best fit, we obtained the two heteronuclear dipolar ^{15}N–^{1}H coupling constants to be $b_{12}/2\pi = 12\,890$ (−440, +460) Hz and $b_{13}/2\pi = 12\,860$ (−460, +440) Hz and the H–N–H bond angle to be $\theta = 112 \pm 2°$. The dipolar couplings correspond to internuclear distances of $r_{12} = 98.1 \pm 1.1$ pm and $r_{13} = 98.2$ (+1.2, −1.1) pm. From the analysis of the two-dimensional 95% confidence area of the parameter pair (b_{12}, b_{13}), we obtain the distance pair $(r_{12}, r_{13}) = (96.8\text{ pm}, 99.5\text{ pm})$ as the one inside the 95% confidence area with the largest difference of $\Delta r = |r_{12} - r_{13}| = 2.7$ pm.

For the NH_2 group at a ^{15}N chemical shift of −290.5 ppm (Fig. 10(c)), we obtained the two heteronuclear dipolar ^{15}N–^{1}H coupling constants to be $b_{12}/2\pi = b_{13}/2\pi = 12\,270$ (−420, +430) Hz and the H–N–H bond angle to be $\theta = 109 \pm 2°$. The dipolar couplings correspond to internuclear distances of $r_{12} = r_{13} = 99.8$ (+1.2, −1.1) ppm. In this case, we obtained the distance pair $(r_{12}, r_{13}) = (98.5\text{ pm}, 100.9\text{ pm})$ as the one inside the 95% confidence area with the largest difference of $\Delta r = 2.4$ pm.

Finally, for the NH_2 group at an ^{15}N chemical shift of −280.0 ppm (Fig. 10(d)), we estimated the two heteronuclear dipolar ^{15}N–^{1}H coupling constants to be $b_{12}/2\pi = 12\,850$ (−450, +500) Hz and $b_{13}/2\pi = 12\,830$ (−480, +470) Hz and the H–N–H bond angle to be $\theta = 113 \pm 2°$. The dipolar couplings correspond to internuclear distances of $r_{12} = 98.2 \pm 1.2$ pm and $r_{13} = 98.3$ (+1.3, −1.2) pm. Here

DOI: 10.1002/mrc

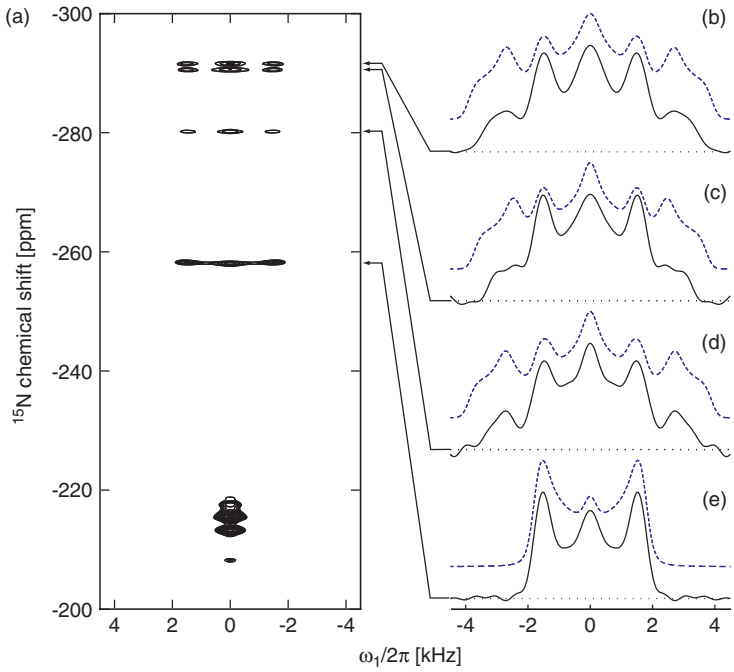

Figure 10. (a) Experimental 2D spectrum of [U-^{15}N]-MP correlating the isotropic ^{15}N chemical shift and the ^{15}N–^{1}H heteronuclear dipolar coupling. The spectrum was recorded using the R18$_2^5$ sequence[21,22] with an ^{1}H rf field of 92.601 kHz at a spinning frequency of 20.578 kHz and an external field of 7.05 T. TPPM decoupling with a ^{1}H nutation frequency of 90 kHz, pulse duration of 5.7 μs and rf phases of ±37° was applied during signal detection. The t_1 evolution time is given by the duration of the R18$_2^5$ sequence, which was incremented in steps of 10.8 μs. A total of 145 increments in t_1 was used. (b)–(e) Sections through the 2D spectrum parallel to the ω_1 axis (solid black lines) shown together with best-fit simulations using the Liouville equation based on the average Hamiltonian (dashed lines). The best-fit results are listed in Table 2. (b) NH_2 group at −291.3 ppm (N7), (c) NH_2 group at −290.5 ppm (N6), (d) NH_2 group at −280.0 ppm (N11) and (e) NH group at −258.0 ppm (N8).

we obtained the distance pair $(r_{12}, r_{13}) = (96.8\ \text{pm}, 99.7\ \text{pm})$ as the one inside the 95% confidence area with the largest difference of $\Delta r = 2.9$ pm.

DISCUSSION

In the following text, we discuss our solid-state NMR results in connection with the structural model of MP shown in Fig. 1(c)–(e). This model was built using X-ray powder diffraction in combination with a molecular modeling Rietveld refinement approach where the results of our solid-state NMR ^{1}H and ^{1}H–X HETCOR spectroscopy had to be considered to elucidate the protonation of the melamine and phosphate moieties.

The ^{15}N 1D spectrum of MP, the ^{15}N–^{1}H 2D HETCOR spectrum and the ^{15}N–^{1}H distance measurements show that the endocyclic nitrogen site leading to the ^{15}N resonance at −258.0 ppm is protonated where the chemical shift of the attached proton is given by 13.7 ppm. This high ^{1}H chemical shift indicates that this proton is hydrogen bonded via a N–H···O=P hydrogen bond to the phosphate moiety. The other two endocyclic nitrogen sites in the melamine molecule are nonprotonated. As a result, the melamine unit is singly positively charged. Hence, in the crystal structure shown in Fig. 1(c), the endocyclic nitrogen N8 is protonated (H21) and therefore the ^{15}N chemical shift of −258.0 ppm is assigned to N8 and the ^{1}H chemical shift of 13.7 ppm is assigned to H21.

The phosphate moiety is doubly protonated (H22 and H23), hence it represents a dihydrogenphosphate unit $H_2PO_4^-$. The 2D homonuclear ^{1}H double-quantum spectrum indicated that pairs of these groups are hydrogen bonded with each other. The hydrogen bonding of the dihydrogenphosphate units is shown in Fig. 1(e). The ^{1}H chemical shift of the proton site interconnecting pairs of phosphate units is given by 11.1 ppm (H22), since these protons appear pairwise close in space to each other, leading to the strong diagonal peak in the ^{1}H double-quantum spectrum. Different pairs of dihydrogenphosphate units are connected by hydrogen bonding via H23; however, these protons do not appear pairwise close in space and are therefore responsible for the ^{1}H resonance at 13.2 ppm. The ^{31}P–^{1}H correlation spectrum is in agreement with this assignment of the two proton sites of the $H_2PO_4^-$ units.

The ^{13}C 1D spectrum and the ^{13}C–^{1}H HETCOR spectrum of MP allow to conclude that the ^{13}C resonance at 156 ppm stems from the two sites C12 and C13 and that the ^{13}C resonance at 164 ppm originates from the site C14.

A further step in assigning the remaining ^{15}N resonances besides the resonance at −258.0 ppm originating from N8 may be undertaken with the help of the ^{15}N double-quantum spectrum. The resonance at −280.0 ppm can be assigned to the site N11 since it shows a close proximity to the resonance of the two nonprotonated endocyclic sites N9 and N10 at −213.3 and −215.6 ppm, where a unique identification of these two resonances is not possible with the help of the

DOI: 10.1002/mrc

MRC

^{15}N double-quantum spectrum alone. The two resonances at −290.5 and −291.3 ppm originate from N6 and N7 where again a unique assignment is not possible at this stage.

Now we would like to discuss further aspects in the assignment of the ^{1}H double-quantum spectrum and the different sections through the ^{15}N–^{1}H spectrum shown in Figs 6 and 7, respectively. On the one hand, the proton H22 resonance at 11.1 ppm shows a strong double-quantum peak with the ^{1}H resonance at 6.2 ppm. This suggests that the latter can be attributed to NH_2 site H17 with the help of the MP model shown in Fig. 1(c) and (d), leaving the assignment of the ^{1}H resonance at 8.0 ppm to H18. On the other hand, the double-quantum peak between proton resonances at 13.7 and about 8.1 ppm in the experimental ^{1}H double-quantum spectrum suggests the opposite assignment of the resonance at 8.0 ppm to H17 and of the resonance at 6.2 ppm to H18. Hence, from the experimental ^{1}H double-quantum spectrum in Fig. 7, the unique assignment of H17 and H18 to the proton chemical shifts of 6.2 and 8.0 ppm is not possible. We attribute this difficulty to possible multiple-spin effects in the dense proton network of MP. However, it follows from Fig. 6(c) that the ^{15}N resonance at −291.3 can be attributed to N7. According to the MP model, H17 has close contacts with both H22 and H23, which is in agreement with the ^{1}H double-quantum spectrum. In addition, due to the double-quantum peak between the proton H23 resonance at 13.2 ppm and the resonance at 6.8 ppm, the latter may be assigned to H19. It follows from Fig. 6(e) that the ^{1}H resonance at 8.7 ppm stems from H20. Finally, ^{15}N resonance at −290.5 ppm may be assigned to N6. According to the MP model, there is a close contact between H21 and H16 and only a double-quantum peak between the H21 resonance at 13.7 ppm and the resonance at 9.1 ppm is in agreement with the ^{1}H double-quantum spectrum. Hence, we assign the ^{1}H resonances at 9.1 and 5.6 ppm to H16 and H15 respectively.

The suggested assignment of all ^{1}H, ^{13}C, ^{15}N and ^{31}P resonances is summarized in Table 1 and Fig. 9(b).

The result from the solid-state NMR distance and angle determination in the different NH and NH_2 groups of MP can be compared with the values found in the model of MP determined X-ray diffraction and Rietveld refinement shown in Fig. 1(c).

We estimated by solid-state NMR the internuclear N8–H21 distance to be $r_{12} = 102.8\ (+0.3, -0.1)$ ppm. This is about 3% larger than the distance of $r_{n-\mathrm{diff}} = 99.8$ pm estimated by the Rietveld refinement of the powder X-ray results. These discrepancies can be explained by the librational motion of the ^{15}N–^{1}H bond vector, as has been shown by Ishii *et al*. and Case *et al*. using molecular dynamics simulations.[43,44] In general, the discrepancies are much larger for direct bonds involving light hydrogen atoms than for direct bonds involving heavier atoms other than hydrogen. Recently, we observed a similar discrepancy in the determination of ^{17}O–^{1}H bond distances[25,26]

In case of the NH_2 groups, we see a clear deviation between the geometries determined by solid-state NMR and the geometries in the model determined by Rietveld refinement. In this model, for the N6–H_2 group the N6–H16 and N6–H15 distances are given by 93.5 pm and 102.1 pm respectively and the H16–N6–H15 bond angle is 122.7°. The difference between the two N–H distances is $\Delta r = 8.6$ pm. In case of the N7–H_2, the N7–H17 and N7–H18 distances are 117.5 pm and 92.0 pm respectively. The H17–N7–H18 bond angle is given by 108.2° and the difference in the two N–H distances is $\Delta r = 25.5$ pm. Finally, for the N11–H_2 group, the N11–H19 and N11–H20 distances are given by 122.0 pm and 77.1 pm. The H19–N11–H20 bond angle is 115.9° and the difference in the two N–H distances is $\Delta r = 44.9$ pm.

Although the analysis of the NMR results supports a difference in the two N–H distances in the NH_2 groups up to 3 pm, there is no justification for the large differences that are present in the X-ray model. In addition, in two cases, the H–N–H bond angle is significantly larger in the X-ray model than is supported by the solid-state NMR results. We conclude that in the Rietveld refinement of the X-ray model a very wide N–H bond distance restraint window has been used in view of the NMR results. This shows the relative insensitivity of the Rietveld refinement to the

Table 1. Suggested chemical shift assignment of MP: (a) ^{1}H, (b) ^{13}C, (c) ^{15}N, and (d) ^{31}P isotropic chemical shifts (δ_{iso}) in MP. The sites are labeled according to the numbering scheme shown in Fig. 1(c).

a ^{1}H Chemical Shifts

Site	Type	δ_{iso} [ppm]
H15	NH_2	5.6
H16	NH_2	9.1
H17	NH_2	6.2/8.0*
H18	NH_2	8.0/6.2*
H19	NH_2	6.8
H20	NH_2	8.7
H21	NH	13.7
H22	$H_2PO_4^-$	11.1
H23	$H_2PO_4^-$	13.2

b ^{13}C Chemical Shifts

Site	Type	δ_{iso} [ppm]
C12, C13	endocyclic	156
C14	endocyclic	164

c ^{15}N Chemical Shifts

Site	Type	δ_{iso} [ppm]
N6	exocyclic, NH_2	−290.5
N7	exocyclic, NH_2	−291.3
N8	endocyclic, NH	−258.0
N9	endocyclic	−213.3
N10	endocyclic	−215.6
N11	exocyclic, NH_2	−280.0

d ^{31}P Chemical Shift

Site	Type	δ_{iso} [ppm]
P1	$H_2PO_4^-$	−0.2

* Values indicate ambiguous assignments.

DOI: 10.1002/mrc

Table 2. Best-fit results for the geometries of the different NH and NH_2 groups in MP obtained for the experimental solid-state NMR results shown as solid lines in Fig. 10(b)–(e). The corresponding best-fit simulations using the Liouville equation based on the average Hamiltonian are shown as dashed lines in Fig. 10(b)–(e)

Site	Type	$b_{12}/2\pi$ [Hz]	$b_{13}/2\pi$ [Hz]	θ [°]	r_{12} [pm]	r_{13} [pm]
N8	NH	11 200 (−85, +27)			102.8 (+0.3, −0.1)	
N6	NH_2	12 270 (−420, +430)	12 270 (−420, +430)	109 ± 2	99.8 (+1.2, −1.1)	99.8 (+1.2, −1.1)
N7	NH_2	12 890 (−440, +460)	12 860 (−460, +440)	112 ± 2	98.1 ± 1.1	98.2 (+1.2, −1.1)
N11	NH_2	12 850 (−450, +500)	12 830 (−480, +470)	113 ± 2	98.2 ± 1.2	98.3 (+1.3, −1.2)

exact proton positions. Hence, solid-state NMR results could in general serve as experimental constraints allowing for a better refinement of the proton positions.

CONCLUSIONS

This study shows the level of structural detail that can be achieved employing state-of-the-art solid-state NMR experiments. Especially the possibility of fast MAS (>45 kHz) at high magnetic fields gives well-resolved proton spectra that in combination with homonuclear correlation and HETCOR experiments provide detailed information about the proton connectivities in a material that is hardly accessible by powder X-ray diffraction data. Specifically, we showed for MP that ^{1}H solid-state single- and double-quantum NMR spectroscopy under fast MAS conditions combined with heteronuclear ^{1}H–^{13}C, ^{1}H–^{31}P and ^{1}H–^{15}N correlation spectroscopy and ^{15}N double-quantum spectroscopy and quantitative ^{15}N–^{1}H distance measurements are very powerful tools to study the structure and hydrogen-bonding properties in these materials. Essential results such as the protonation of the melamine moieties and the geometries of the NH and NH_2 groups can only be convincingly obtained by solid-state NMR. Rietveld refinement of data obtained by X-ray power diffraction alone was not capable of producing geometries that are in agreement with our solid-state NMR results. We therefore suggest that solid-state NMR results are routinely included in the process of Rietveld refinement. Our solid-state NMR results are of great importance in general for the study of the mechanism of melamine phosphates as a flame retardant in actual polymer materials. To elucidate structural arrangements of MP and related flame retardants under combustion tests in an actual polymer matrix, one has to deal with inherently disordered materials. As solid-state NMR probes local rather than long-range order, it can still provide information about the interaction of the flame retardant with the polymer matrix and probe conversion of the material as a result of the heat exposure. Such studies will allow the improvement of environmental friendly flame retardants based on melamine phosphates in the future.

MATERIALS AND METHODS

Sample

The ^{13}C and ^{15}N enriched samples of MP ([U-^{13}C]-MP and [U-^{15}N]-MP respectively) have been prepared by DSM (Geleen, The Netherlands). In the first step, [U-^{13}C]-melamine and [U-^{15}N]-melamine were synthesized from [97% U-^{13}C]-urea and [97% U-^{15}N]-urea respectively. The labeled urea was purchased from Aldrich. In the second step, MP was synthesized. A mixture of either ^{13}C or ^{15}N enriched melamine with water was heated to 75 °C. Phosphoric acid was added to this mixture while stirring. The resulting reaction mixture was stirred for 2 h at 75 °C. The solvent was evaporated under vacuum at 80 °C leaving MP.

Solid-state NMR

All experiments were performed at static magnetic fields of 7.05 and 18.8 T using a Varian Infinity and Infinity+ console respectively. The experiments at 18.8 T were done using a homebuilt double-resonance MAS probehead utilizing a Samoson 1.8 mm stator.[29] The experiments at 7.05 T were all performed employing a double-resonance Bruker MAS probehead with a 2.5 mm stator. The sample compartment had an inner diameter of 1.3 mm and was restricted in length by Teflon spacers to about 8.4 mm, leading to a sample volume of about 11 μl.

High-resolution ^{1}H spectroscopy

The experimental single-pulse ^{1}H MAS spectrum shown in Figs 2(a), 3(a), 4(a), 5(a) and 6(a) was recorded at a static field of 18.8 T and a sample spinning frequency of 49.1 kHz.

Heteronuclear correlation spectroscopy

The experimental 2D HETCOR spectra shown in Figs 3(b), 4(b), 4(c), 5(b), 5(c) and 6(b) were acquired at a static field of 7.05 T and a spinning frequency of 12 kHz using the pulse sequence shown in Fig. 11(a) where S corresponds to ^{13}C, ^{15}N or ^{31}P.

During the time interval t_1, a homonuclear decoupling sequence is applied. We chose the FSLG scheme for this purpose.[45–47] We compared the sequences FSLG,[45–47] PMLG[48–50] and $R18_2^9$ (Ref. 51) by taking ^{1}H spectra of L-alanine, but neither PMLG nor $R18_2^9$ showed an improved performance (better-resolved ^{1}H spectra) compared to FSLG on the spectrometer console used (Chemagnetics Infinity).

After the ^{1}H transverse magnetization is evolved during the interval t_1, it is transferred to the S-spins by ramped CP.[52] The ^{1}H rf field during the CP is set off resonance, so as to satisfy the Lee–Goldburg condition,[53,54] in order to achieve homonuclear decoupling of the ^{1}H during CP.[55–57] This ensures pure heteronuclear magnetization transfer via the heteronuclear dipolar couplings.

During the LG-CP, the rf amplitudes were adjusted in all cases so that the difference of the ^{1}H nutation frequency and the S-spin nutation frequency was exactly equal to the spinning frequency (the −1 LG-CP sideband condition).[56,57]

DOI: 10.1002/mrc

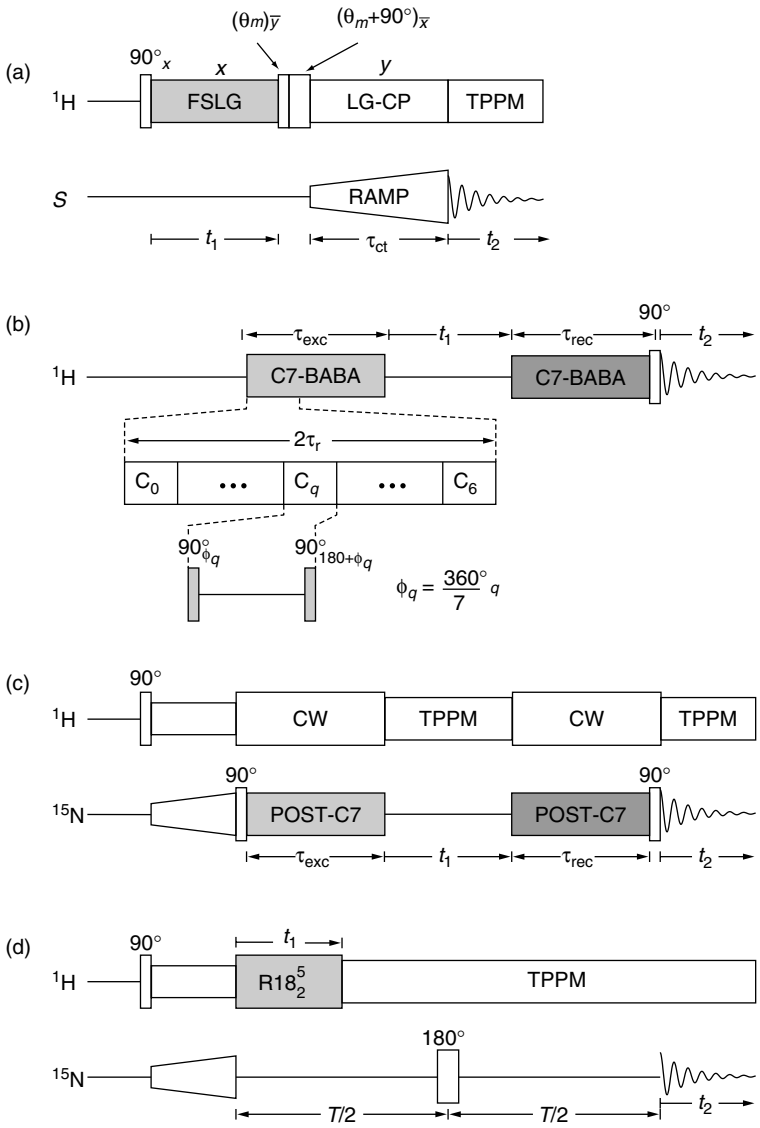

Figure 11. (a) Rf pulse sequence to obtain 2D HETCOR MAS spectra between ^{1}H and spin species S (^{13}C, ^{15}N, ^{31}P), where the ω_1 axis in the resulting 2D spectrum corresponds to the high-resolution ^{1}H dimension achieved by the homonuclear decoupling sequence FSLG and the ω_2 axis corresponds to the direct S-spin dimension. θ_m indicates an rf pulse with the flip angle 54.74° (magic angle). (b) Rf pulse sequence used to record 2D homonuclear double-quantum ^{1}H spectra. The C7 sequence employing the BABA basic element is used to excite and reconvert homonuclear ^{1}H double-quantum coherences. (c) Rf pulse sequence to obtain 2D homonuclear double-quantum ^{15}N spectra. The POST-C7 sequence is used to create and reconvert homonuclear ^{15}N double-quantum coherences. (d) Rf pulse sequence to estimate ^{15}N–^{1}H internuclear distances. The $R18_2^5$ sequence is employed to recouple ^{15}N–^{1}H heteronuclear dipolar couplings.

The S-spin transverse magnetization is detected in the subsequent interval t_2 while strong TPPM decoupling[58] is applied to the ^{1}H. The ω_1 axis of the resulting 2D spectrum $S(\omega_1, \omega_2)$ corresponds to the high-resolution indirect ^{1}H dimension, whilst the ω_2 axis corresponds to the direct S-spin dimension.

Under the FSLG homonuclear decoupling sequence, the isotropical chemical shift of the ^{1}H is scaled theoretically by a factor $\kappa = 1/\sqrt{3} = 0.57$. We determined the scaling factor experimentally ahead of each experiment by acquiring a series of two-dimensional ^{1}H spectra by choosing different offsets for the rf carrier frequency. The experimentally determined values for the scaling factors were used to correct the scaling of the ^{1}H chemical shift dimension.

Homonuclear double-quantum ^{1}H spectroscopy

The experimental 2D homonuclear double-quantum ^{1}H spectrum shown in Fig. 7 was acquired at a static field of 18.8 T and a spinning frequency of 50 kHz using the pulse sequence shown in Fig. 11(b). Longitudinal ^{1}H magnetization is converted into double-quantum coherence by a C7 sequence[39] of duration τ_{exc}. The basic element of the C7 sequence was the $90_0-\tau-90_{180}$ cycle that is also the basis of the BABA sequence.[40,41] Therefore, the resulting homonuclear double-quantum recoupling sequence is denoted C7-BABA. To comply with the requirements of the C7 sequence, the basic BABA element has a duration of $\tau_E = 2\tau_r/7$, where τ_r is the sample rotation period. The excited ^{1}H double-quantum coherences are allowed to evolve for an interval t_1,

DOI: 10.1002/mrc

and are reconverted into longitudinal ^{1}H magnetization by applying another C7-BABA sequence of duration τ_{rec} that is phase shifted by 90° with respect to the excitation sequence. The longitudinal magnetization is converted into observable magnetization by a 90° read pulse. The ^{1}H NMR signal is detected in the subsequent time interval t_2. The reconversion C7-BABA sequence and the read pulse are phase cycled together in four steps to select double-quantum coherence during the t_1 interval. In addition, the read pulse is phase cycled in four steps to select longitudinal magnetization before the read pulse. In order to allow for arbitrary t_1 increments, the rf phase of the reconversion C7-BABA sequence is adjusted as a function of t_1 according to the time–phase relationship.[17,59] A two-dimensional data matrix $s(t_1, t_2)$ is compiled by acquiring a set of transients with incrementation of the interval t_1. The data matrix $s(t_1, t_2)$ is subjected to a complex Fourier transform in the t_2 dimension, and a cosine Fourier transform in the t_1 dimension, in order to obtain the 2D spectrum $S(\omega_1, \omega_2)$. We employed the the time-proportional phase incrementation (TPPI) procedure for separating the (±2) quantum signals.[60] The ω_1 axis of the resulting spectrum corresponds to the double-quantum ^{1}H dimension, whilst the ω_2 axis corresponds to the single-quantum ^{1}H dimension.

We used a 90° ^{1}H pulse of duration 2.1 μs in the BABA basic element that had a total duration of $\tau_E = 5.71$ μs. The intervals for exciting and reconverting double-quantum coherence were each given by 40 μs corresponding to two rotational periods, i.e. a single complete C7-BABA block.

Homonuclear double-quantum ^{15}N spectroscopy

The experimental 2D homonuclear double-quantum ^{15}N spectrum shown in Fig. 8 was acquired at a static field of 7.05 T and a spinning frequency of 6.056 kHz using the pulse sequence shown in Fig. 11(c) employing the POST-C7 homonuclear double-quantum recoupling sequence.[42] Ramped cross-polarization followed by a 90° pulse creates enhanced ^{15}N longitudinal magnetization that is converted into double-quantum coherence by a POST-C7 sequence of duration τ_{exc}. The ^{15}N double-quantum coherences are allowed to evolve for an interval t_1, and are reconverted into longitudinal ^{15}N magnetization by applying another POST-C7 sequence of duration τ_{rec}. The longitudinal magnetization is converted into observable magnetization by a 90° read pulse. The phase cycling and data processing were the same as discussed in the previous section for the case of homonuclear double-quantum ^{1}H spectroscopy.

The ^{15}N rf field during the POST-C7 sequence was given by 42.4 kHz and the intervals for exciting and reconverting double-quantum coherence were each set to 7.9 ms corresponding to 48 rotational periods, i.e. 24 complete POST-C7 blocks. Continuous-wave decoupling with a ^{1}H nutation frequency of 120 kHz was applied during the POST-C7 sequence and TPPM decoupling with a nutation frequency of 100 kHz, pulse duration of 4.9 μs and rf phases of ±35° was used during signal detection.

^{15}N–^1H distance measurements

The experimental 2D spectrum shown in Fig. 10 correlating the isotropic ^{15}N chemical shift and the ^{15}N–^{1}H heteronuclear dipolar coupling was recorded at a spinning frequency of 20.578 kHz and an external field of 7.05 T using the pulse sequence shown in Fig. 11(d).[21,22] Ramped cross-polarization creates enhanced ^{15}N transverse magnetization that is subjected to a Hahn echo sequence of total duration T and a 180° pulse as refocusing pulse in the center of the evolution time interval. For a time t_1, the ^{15}N transverse magnetization evolves in the presence of the $R18_2^5$ heteronuclear recoupling sequence on the protons.[21,22] For the remaining time of the Hahn echo, TPPM decoupling is applied. In the t_1 dimension, we applied a Gaussian apodization function with a width of 400 Hz. The ω_1 axis of the resulting 2D spectrum $S(\omega_1, \omega_2)$ corresponds to the ^{15}N–^{1}H dipolar coupling dimension, whilst the ω_2 axis corresponds to the direct ^{15}N dimension.

The theory of the heteronuclear recoupling sequence $R18_2^5$ has been discussed in detail before.[21,61] In order to discuss how we obtained the simulated results shown in Fig. 10(b)–(e) for the ^{15}N–^{1}H heteronuclear recoupling experiment, we briefly outline the underlying theoretical considerations. Consider a spin-1/2 system consisting of a single S-spin (^{15}N) and several I-spins (^{1}H). The first-order heteronuclear average Hamiltonian for the $R18_2^5$ sequence is given by:[61]

$$\bar{H}_{IS}^{(1)} = \sum_j \frac{1}{2}\omega_{jS}\, 2I_{j\psi}S_z \tag{1}$$

where the recoupled dipolar frequencies ω_{jS} are defined as positive real numbers

$$\omega_{jS} = 2|b_{jS}||\kappa|\sqrt{2}\sum_{m=-2}^{2} d_{0m}^{(2)}(\beta_{PM}^{jS}) d_{m2}^{(2)}(\beta_{MR}) e^{-im(\gamma_{PM}^{jS}+\alpha_{MR})} \tag{2}$$

The dipolar coupling constant b_{jS} is related to the internuclear distance r_{jS} and the gyromagnetic ratios γ_S and γ_I by $b_{jS} = -(\mu_0/4\pi)\gamma_S\gamma_I\hbar r_{jS}^{-3}$. The Euler angles $\Omega_{PM}^{jS} = \{\alpha_{PM}^{jS}, \beta_{PM}^{jS}, \gamma_{PM}^{jS}\}$ describe the transformation of each heteronuclear dipolar coupling from its principal axis system to a molecule fixed frame. The Euler angles $\Omega_{MR} = \{\alpha_{MR}, \beta_{MR}, \gamma_{MR}\}$ relate the molecular frame to a frame fixed on the rotor, and are random variables in a powder. It should be noted that the frequencies ω_{jS} only depend on the Euler angles α_{MR} and β_{MR}. This property is referred to as γ-encoding.[62] κ is the scaling factor of the heteronuclear recoupling sequence and for $R18_2^5$ it is given by $\kappa = 27\sqrt{3}\sin(5\pi/8)/(65\pi) \approx 0.1754$. The spin operator $I_{j\psi}$ denotes a rotated I_{jx} spin operator[20,61]

$$I_{j\psi} = \exp\{-i\psi_{IS}I_z\} I_{jx} \exp\{i\psi_{IS}I_z\} \tag{3}$$

where $I_z = \sum_j I_{jz}$ is the operator of the z-component of the total I-spin angular momentum. The rotation angle ψ_{IS} depends on the Euler angle γ_{MR} and the sign of the scaling factor κ and the sign of the heteronuclear couplings b_{jS}. If we assume that all heteronuclear dipolar couplings are of the same type, the angle ψ_{IS} for a certain molecular orientation Ω_{MR} is given by

$$\psi_{IS} = \arg(b_{jS}) + \arg(\kappa) - 2\gamma_{MR} \tag{4}$$

For the case of ^{15}N–^{1}H heteronuclear recoupling, $b_{jS} \geq 0$ and therefore $\arg(b_{jS}) = 0$. Furthermore, $\arg(\kappa) = 0$ for $R18_2^5$.

DOI: 10.1002/mrc

The average Hamiltonian in Eqn (1) is a single-quantum average Hamiltonian in the *I*-spin operators. Therefore, $R18_2^5$ is referred to as a single-quantum recoupling sequence. An important property of these sequences is that different recoupled heteronuclear dipolar interactions sharing a single site do not commute. This property is referred to as 'dipolar truncation'.[63] On the one hand, this prevents the measurement of a weak dipolar coupling between two spins if one or both spins are also strongly dipolar coupled to other spins. On the other hand, this property allows to determine H–C–H and H–N–H bond angles in CH_2 and NH_2 groups respectively. The $R18_2^5$ sequence recouples the *I*-spin chemical shift anisotropy (CSA) in first order as well. However, Zhao *et al*. have shown that the *I*-spin CSA only influences the central peak in the *S*-spin dipolar lineshape and does not affect the characteristic dipolar splitting due to the heteronuclear dipolar coupling.[21,22] Therefore, we have ignored the *I*-spin CSA in our discussion of the properties of the $R18_2^5$ sequence and the analysis of N–H distance measurements.

It should be noted that other types of heteronuclear recoupling sequences exist that are not affected by the *I*-spin CSA since they lead to a longitudinal two-spin-order (I_zS_z) average Hamiltonian for the heteronuclear dipolar coupling in first order that commutes with the *I*-spin CSA terms. Examples are REDOR,[64,65] which do not accomplish homonuclear decoupling, and the $SR4_1^2$ sequence recently introduced by us and its related sequences such as $SR12_3^5$ and $SR32_8^{15}$ (Refs. 25, 26) that achieve homonuclear decoupling at the same time as recoupling the heteronuclear dipolar interactions. Since these sequences do not suffer from dipolar truncation, they are well suited to determine weak heteronuclear dipolar couplings in the present of strong ones.[26] However, as a result they do not allow to determine H–C–H and H–N–H bond angles in CH_2 and NH_2 groups.

The evolution of a heteronuclear spin system under the first order single-quantum average Hamiltonian in Eqn (1) for the $R18_2^5$ sequence has been discussed in Hilbert space in Ref. 61. However, in order to include relaxation of the spin system during the heteronuclear recoupling sequence, we chose a simple average Liouvillian approach.[20] In general, the Liouville equation for the evolution of the spin system under the average Hamiltonian $\bar{H}_{IS}^{(1)}$ in superoperator formalism can be written as

$$\frac{d}{dt}|\rho(t)) = \{-i\hat{\bar{H}}^{comm} - \hat{\Gamma}\}|\rho(t)) \quad (5)$$

$$= \hat{\Omega}|\rho(t)) \quad (6)$$

where $|\rho(t))$ is the superoperator of the density matrix, $\hat{\Gamma}$ is the relaxation superoperator and $\hat{\bar{H}}^{comm}$ denotes the commutation superoperator[66] of the average Hamiltonian $\bar{H}_{IS}^{(1)}$, i.e. $\hat{\bar{H}}^{comm}|A) = |[\bar{H}_{IS}^{(1)}, A])$.[66] The superoperator $\hat{\Omega}$ is given by

$$\hat{\Omega} = -i\hat{\bar{H}}^{comm} - \hat{\Gamma}$$

Consider now the pulse sequence shown in Fig. 11(d). The integrated amplitude of the *S*-spin signal as a function of the evolution interval t_1 for a certain molecular orientation Ω_{MR} may in general be written as

$$s(t_1, \Omega_{MR}) = \frac{(S_x|\hat{U}(t_1, \Omega_{MR})|S_x)}{(S_x|S_x)} \quad (8)$$

where $\hat{U}(t_1, \Omega_{MR})$ is the propagation superoperator

$$\hat{U}(t_1, \Omega_{MR}) = \exp\{\hat{\Omega}t_1\} \quad (9)$$

The amplitudes in Eqn (8) depend on the orientation Ω_{MR}. In a powder, the orientational average is observed

$$s(t_1) = \frac{1}{8\pi^2}\int_0^{2\pi} d\alpha_{MR}\int_0^{\pi} d\beta_{MR}\sin\beta_{MR}\int_0^{2\pi} d\gamma_{MR}s(t_1, \Omega_{MR}) \quad (10)$$

It should be noted that in the case of a γ-encoded average Hamiltonian as the one in Eqn (1) for the $R18_2^5$ sequence, the powder averaging only has to be done over the powder angles α_{MR} and β_{MR}.

In the case of a heteronuclear two-spin system consisting of two spins denoted *S* and I_1, the relevant Liouville subspace is spanned by the superoperators $|1) = |S_x)$ and $|2) = |2I_{1\psi}S_y)$ and the superoperator $\hat{\Omega}$ in this basis is given by

$$\hat{\Omega} = \begin{pmatrix} -R_S & -\omega_{1S}/2 \\ \omega_{1S}/2 & -R_{IS} \end{pmatrix} \quad (11)$$

where the matrix elements are given by $\hat{\Omega}_{jk} = (j|\hat{\Omega}|k)$ with $j, k = 1, 2$. R_S and R_{IS} are the relaxation rate constants of the states $|S_x)$ and $|2I_{1\psi}S_y)$ respectively. Cross-relaxation between different superoperator states has been ignored. The frequency ω_{1S} is given by Eqn (2).

In the case of a heteronuclear three-spin system consisting of three spins denoted *S*, I_1 and I_2, the relevant Liouville subspace is spanned by the superoperators $|1) = |S_x)$, $|2) = |2I_{1\psi}S_y)$, $|3) = |2I_{2\psi}S_y)$, and $|4) = |4I_{1\psi}I_{2\psi}S_x)$ and the superoperator $\hat{\Omega}$ in this basis is given by

$$\hat{\Omega} = \begin{pmatrix} -R_S & -\omega_{1S}/2 & -\omega_{2S}/2 & 0 \\ \omega_{1S}/2 & -R_{IS} & 0 & \omega_{2S}/2 \\ \omega_{2S}/2 & 0 & -R_{IS} & \omega_{1S}/2 \\ 0 & -\omega_{2S}/2 & -\omega_{1S}/2 & -R_{IIS} \end{pmatrix} \quad (12)$$

where the matrix elements are given by $\hat{\Omega}_{jk} = (j|\hat{\Omega}|k)$ with $j, k = 1, \ldots, 4$. R_{IIS} is the relaxation rate constant of the state $|4I_{1\psi}I_{2\psi}S_x)$. For the states $|2I_{1\psi}S_y)$ and $|2I_{2\psi}S_y)$, the same relaxation rate constant R_{IS} is assumed. The frequencies ω_{1S} and ω_{2S} are given by Eqn (2).

The propagator $\hat{U}(t_1, \Omega_{MR})$ in Eqn (9) can be calculated by matrix diagonalization of $\hat{\Omega}$. Although in the case of a two-spin system this may be done analytically, in the general case of a multiple-spin system this has to be done numerically. For all calculations, powder averaging was accomplished using a set of 987 pairs of $\{\alpha_{MR}, \beta_{MR}\}$ angles chosen according to the ZCW scheme.[67]

In case of the calculations for the NH groups, a two-spin system consisting of a single ^{15}N and a single ^{1}H site was assumed and Eqns (11) and (8) were used to calculate the modulation of the ^{15}N signal as the function of t_1. The Fourier transformed calculations were fitted to the experimental spectrum shown in Fig. 10(e), where areas around

DOI: 10.1002/mrc

the characteristic peaks at about ±1.5 kHz were selected to determine the root-mean-squared deviation between calculated and experimental results. The fitting parameters were the heteronuclear $^{15}N-^{1}H$ dipolar coupling b_{12} and the two relaxation rate constants R_S and R_{IS}, i.e. a total of three fitting parameters were used.

In case of the calculations for the NH_2 groups, a three-spin system consisting of a single ^{15}N and a two ^{1}H sites was assumed and Eqns (12) and (8) were used to calculate the modulation of the ^{15}N signal as the function of t_1. The Fourier transformed calculations were fitted to the experimental spectra shown in Fig. 10(b)–(d), where areas around the characteristic peaks at about ±1.5 and ±2.7 kHz were selected to determine the root-mean-squared deviation between calculated and experimental results. The fitting parameters were the two heteronuclear $^{15}N-^{1}H$ dipolar couplings b_{12} and b_{13}, the H–N–H bond angle θ and the three relaxation rate constants R_S, R_{IS} and R_{IIS}, i.e. a total of six fitting parameters were used.

We obtained the 95% confidence interval for a single parameter p (e.g. $p = b_{12}$) by calculating the root-mean-squared deviation RMS for a series of different values for p, where the other fitting parameters were optimized as to minimize RMS in each case. The 95% confidence interval is determined by the set of values for p for which $\mathrm{RMS} \leq \mathrm{RMS}_{\min}\{1 + F^{0.05}_{1,n_e-n_f}/(n_e - n_f)\}$, where $\mathrm{RMS}_{\min}$ is the root-mean-squared deviation between experimental and simulated spectra minimized by optimizing all n_f fitting parameters ($n_f = 3, 6$) and n_e is the number of experimental points used in the fit. $F^{\alpha}(p_1, p_2)$ is the upper α probability point of the F distribution with p_1 and p_2 degrees of freedom.[68]

In case of the NH_2 calculations, we obtained in addition the two-dimensional 95% confidence area for the parameter pair (b_{12}, b_{13}) by calculating the root-mean-squared deviation RMS on a two-dimensional grid of values for (b_{12}, b_{13}), where the other fitting parameters were optimized as to minimize RMS in each case. The 95% confidence area is determined by the set of pairs (b_{12}, b_{13}) for which $\mathrm{RMS} \leq \mathrm{RMS}_{\min}\{1 + F^{0.05}_{2,n_e-6}/(n_e - 6)\}$, where $\mathrm{RMS}_{\min}$ is the root-mean-squared deviation between experimental and simulated spectra minimized by optimizing all 6 fitting parameters and n_e is the number of experimental points used in the fit.

Acknowledgements

The authors would like to thank Ernst van Eck, Tom Bloemberg, Marco Tessari, Jan van Os, Hans Janssen and Gerrit Janssen for discussions and experimental help, and Adri Klaassen for preliminary NMR work. In addition, the authors thank Vladimir Brodski, Dirk De Ridder, René Peschar and Henk Schenk from the Laboratory for Crystallography, HIMS, University of Amsterdam, Ad Braam, Betty Coussens and Shahab Jahromi from DSM, and Nico Aelmans from Ciba Speciality Chemicals for helpful discussions. The authors also thank DSM in Geleen, The Netherlands for the preparation of the MP samples. This research was supported through the BTS program in collaboration with DSM and Ciba Speciality Chemicals.

REFERENCES

1. Lu S-Y, Hamerton I. *Prog. Polym. Sci.* 2002; **27**: 1661.
2. Zaikov GE, Lomakin SM. *J. Appl. Polym. Sci.* 2002; **86**: 2449.
3. Santillo D, Johnston P. *Environ. Int.* 2003; **29**: 725.
4. Horacek H, Grabner R. *Polym. Degrad. Stabil.* 1996; **54**: 205.
5. Bann B, Miller SA. *Chem. Rev.* 1958; **58**: 131.
6. Hughes EW. *J. Am. Chem. Soc.* 1941; **63**: 1737.
7. Varghese JN, O'Connell AM, Maslen EN. *Acta Crystallogr.* 1977; **B33**: 2102.
8. Marchewka MK, Pietraszko A. *J. Phys. Chem. Solids* 2003; **64**: 2169.
9. Desiraju GR, Steiner T. *The Weak Hydrogen Bond in Structual Chemistry and Biology, International Union of Crystallography Monographs on Crystallography 9*. Oxford University Press: New York, 2001.
10. Cichy B, Łuczkowska D, Nowak M, Władyka-Przybylak M. *Ind. Eng. Chem. Res.* 2003; **42**: 2897.
11. Ridder DJAD, Goubitz K, Brodski V, Peschar R, Schenk H. *Helv. Chim. Acta* 2004; **87**: 1894.
12. Janczak J, Perpétuo GJ. *Acta Crystallogr.* 2002; **C58**: o455.
13. Brodski V, Peschar R, Schenk H, Brinkmann A, van Eck ERH, Kentgens APM, Coussens B, Braam A. *J. Phys. Chem. B* 2004; **108**: 15069.
14. Brodski V, Peschar R, Schenk H, Brinkmann A, Bloemberg TG, van Eck ERH, Kentgens APM. *J. Phys. Chem. B* 2005; **109**: 13529.
15. Bennett AE, Griffin RG, Vega S. *NMR Basic Principles and Progress* 1994; **33**: 1.
16. Dusold S, Sebald A. *Annu. Rep. NMR Spectrosc.* 2000; **41**: 185.
17. Levitt MH. Symmetry-based pulse sequences in magic-angle spinning solid-state NMR. In *Encyclopedia of Nuclear Magnetic Resonance*, vol. 9, Grant DM, Harris RK (eds). Wiley: Chichester, 2002.
18. Schnell I. *Prog. Nucl. Magn. Reson. Spectrosc.* 2004; **45**: 145.
19. Hughes C, Baldus M. *Annu. Rep. NMR Spectrosc.* 2005; **55**: 121.
20. Hohwy M, Jaroniec CP, Reif B, Rienstra CM, Griffin RG. *J. Am. Chem. Soc.* 2000; **122**: 3218.
21. Zhao X, Edén M, Levitt MH. *Chem. Phys. Lett.* 2001; **342**: 353.
22. Zhao X, Sudmeier JE, Bachovchin WW, Levitt MH. *J. Am. Chem. Soc.* 2001; **123**: 11097.
23. Schulz-Dobrick M, Metzroth T, Spiess HW, Gauss J, Schnell I. *ChemPhysChem* 2005; **6**: 315.
24. van Beek JD, Dupree R, Levitt MH. *J. Magn. Reson.* 2006; **179**: 38.
25. Brinkmann A, Kentgens APM. *J. Phys. Chem. B* 2006; **110**: 16089.
26. Brinkmann A, Kentgens APM. *J. Am. Chem. Soc.* 2006; **128**: 14758.
27. Caravatti P, Bodenhausen G, Ernst RR. *Chem. Phys. Lett.* 1982; **89**: 363.
28. Brown SP, Spiess HW. *Chem. Rev.* 2001; **101**: 4125.
29. Samoson A, Tuherm T, Gan Z. *Solid State Nucl. Magn. Reson.* 2001; **20**: 130.
30. Goward GR, Sebastiani D, Schnell I, Spiess HW, Kim H-D, Ishida H. *J. Am. Chem. Soc.* 2003; **125**: 5792.
31. Schnell I, Langer B, Söntjens SHM, Sijbesma RP, van Genderen MHP, Spiess HW. *Phys. Chem. Chem. Phys.* 2002; **4**: 3750.
32. Damodaran K, Sanjayan GJ, Rajamohanan PR, Ganapathy S, Ganesh KN. *Org. Lett.* 2001; **3**: 1921.
33. Jürgens B, Irran E, Senker J, Kroll P, Müller H, Schnick W. *J. Am. Chem. Soc.* 2003; **125**: 10288.
34. Lotsch BV, Schnick W. *Chem. Eur. J.* 2007; **13**: 4956.
35. Lotsch BV, Döblinger M, Sehnert J, Seyfarth L, Senker J, Oeckler O, Schnick W. *Chem. Eur. J.* 2007; **13**: 4969.
36. Sattler A, Seyfarth L, Senker J, Schnick W. *Z. Anorg. Allg. Chem.* 2005; **631**: 2545.
37. Jahromi S, Gabriëlse W, Braam A. *Polymer* 2003; **44**: 25.
38. Orr RM, Duer MJ. *Solid State Nucl. Magn. Reson.* 2006; **30**: 130.
39. Lee YK, Kurur ND, Helmle M, Johannessen OG, Nielsen NC, Levitt MH. *Chem. Phys. Lett.* 1995; **242**: 304.
40. Feike M, Demco DE, Graf R, Gottwald J, Hafner S, Spiess HW. *J. Magn. Reson. A* 1996; **122**: 214.
41. Feike M, Graf R, Schnell I, Jäger C, Spiess HW. *J. Am. Chem. Soc.* 1996; **118**: 9631.
42. Hohwy M, Jakobsen HJ, Edén M, Levitt MH, Nielsen NC. *J. Chem. Phys.* 1998; **108**: 2686.
43. Ishii Y, Terao T, Hayashi S. *J. Chem. Phys.* 1997; **107**: 2760.

44. Case DA. *J. Biomol. NMR* 1999; **15**: 95.
45. Mehring M, Waugh JS. *Phys. Rev. B* 1972; **5**: 3459.
46. Bielecki A, Kolbert AC, Levitt MH. *Chem. Phys. Lett.* 1989; **155**: 341.
47. Levitt MH, Kolbert AC, Bielecki A, Ruben DJ. *Solid State Nucl. Magn. Reson.* 1993; **2**: 151.
48. Ashida J, Rice D. *Magn. Moments* 1996; **8**: 19, a Varian publication.
49. Fung BM, Ermolaev K, Yu Y. *J. Magn. Reson.* 1999; **138**: 28.
50. Vinogradov E, Madhu PK, Vega S. *Chem. Phys. Lett.* 1999; **314**: 443.
51. Madhu PK, Zhao X, Levitt MH. *Chem. Phys. Lett.* 2001; **346**: 142.
52. Metz G, Wu X, Smith SO. *J. Magn. Reson. A* 1994; **110**: 219.
53. Goldburg WI, Lee M. *Phys. Rev. Lett.* 1963; **11**: 255.
54. Lee M, Goldburg WI. *Phys. Rev.* 1965; **140**: A1261.
55. Ramamoorthy A, Wu CH, Opella SJ. *J. Magn. Reson.* 1999; **140**: 131.
56. van Rossum B-J, de Groot CP, Ladizhansky V, Vega S, de Groot HJM. *J. Am. Chem. Soc.* 2000; **122**: 3465.
57. Ladizhansky V, Vega S. *J. Chem. Phys.* 2000; **112**: 7158.
58. Bennett AE, Rienstra CM, Auger M, Lakshmi KV, Griffin RG. *J. Chem. Phys.* 1995; **103**: 6951.
59. Brinkmann A, Edén M, Levitt MH. *J. Chem. Phys.* 2000; **112**: 8539.
60. Ernst RR, Bodenhausen G, Wokaun A. *Principles of Nuclear Magnetic Resonance in One and Two Dimensions*, *International Series of Monographs on Chemistry 14*. Oxford University Press: Oxford, 1997.
61. Zhao X, Hoffbauer W, Schmedt auf der Günne J, Levitt MH. *Solid State Nucl. Magn. Reson.* 2004; **26**: 57.
62. Nielsen NC, Bildsøe H, Jakobsen HJ, Levitt MH. *J. Chem. Phys.* 1994; **101**: 1805.
63. Baldus M, Meier BH. *J. Magn. Reson.* 1997; **128**: 172.
64. Gullion T, Schaefer J. *J. Magn. Reson.* 1989; **81**: 196.
65. Gullion T, Vega AJ. *Prog. Nucl. Magn. Reson. Spectrosc.* 2005; **47**: 123.
66. Jeener J. *Adv. Magn. Reson.* 1982; **10**: 1.
67. Cheng VB, Henry H. Suzukawa J, Wolfsberg M. *J. Chem. Phys.* 1973; **59**: 3992.
68. Seber GAF, Wild CJ. *Nonlinear Regression*. Wiley Series in Probability and Statistics Wiley-Interscience: Hoboken, 2003.

DOI: 10.1002/mrc